ACS OMEGA

Open Access

http://pubs.acs.org/journal/acsodf

Article

Quantification of Lanthanides on a PMMA Microfluidic Device with Three Optical Pathlengths Using PCR of UV−Visible, NIR, and Raman Spectroscopy

Hope E. Lackey,*[,⊥] Alyssa F. Espley,[⊥] Savannah M. Potter, Fabrice Lamadie, Manuel Miguirditchian, Gilbert L. Nelson, Samuel A. Bryan,* and Amanda M. Lines*

Cite This: *ACS Omega* 2024, 9, 38548−38556

Read Online

ACCESS | Metrics & More | Article Recommendations | Supporting Information

ABSTRACT: Microfluidic devices (MFDs) offer customizable, low-cost, and low-waste platforms for performing chemical analyses. Optical spectroscopy techniques provide nondestructive monitoring of small sample volumes within microfluidic channels. Optical spectroscopy can probe speciation, oxidation state, and concentration of analytes as well as detect counterions and provide information about matrix composition. Here, ultraviolet−visible (UV−vis) absorbance, near-infrared (NIR) absorbance, and Raman spectroscopy are utilized on a custom poly(methyl methacrylate) (PMMA) MFD for the detection of three lanthanide nitrates in solution. Absorbance spectroscopies are conducted across three pathlengths using three portions of a contiguous channel within the MFD. Univariate and chemometric multivariate modeling, specifically Beer's law regression and principal component regression (PCR), respectively, are utilized to quantify the three lanthanides and the nitrate counterion. Models are composed of spectra from one or multiple pathlengths. Models are also constructed from multiblock spectra composed of UV−vis, NIR, and Raman spectra at one or multiple pathlengths. Root-mean-square errors (RMSE), limit of detection (LOD), and residual predictive deviation (RPD) values are compared for univariate, multivariate, multi-pathlength, and multiblock models. Univariate modeling produces acceptable results for analytes with a simple signal, such as samarium cations, producing an LOD of 5.49 mM. Multivariate and multiblock models produce enhanced quantification for analytes that experience spectral overlap and interfering nonanalyte signals, such as holmium, which had an LOD reduction from 7.21 mM for the univariate model down to 3.96 mM for the multiblock model. Multi-pathlength models are developed that maintain model errors in line with single-pathlength models. Multi-pathlength models have RPDs from 9.18 to 46.4, while incorporating absorbance spectra collected at optical paths of up to 10-fold difference in length.

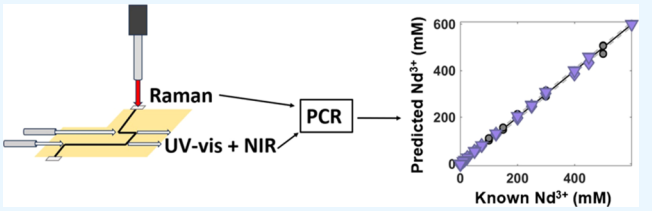

INTRODUCTION

Volume, cost, and time are all variables that influence and constrain the design of experiments and the analysis methods. Microfluidics offers a means to reduce these parameters[1] while providing similar results to lab-scale operations and improving the environmental footprint of processes by reducing waste.[2,3] These benefits are particularly salient for applications such as point-of-care diagnosis,[1] in which samples may be limited in volume and availability. Microfluidics are also desirable for the analysis of hazardous or expensive materials,[4] in which reduced sample volumes limit the monetary, health, and environmental costs that may be incurred by working with and accumulating large sample and waste volumes. Microfluidic devices (MFDs) have been used for small volume analysis of chemical reactions, including kinetics and interfacial chemistries.[3,5,6]

Optical spectroscopy on MFDs grants the ability to conduct real-time sample analysis for lab-on-a-chip applications.[5,7,8] Optical spectroscopy can be used to measure small sample volumes from a microfluidic device as an alternative to or before samples are routed to destructive techniques, such as mass spectrometry.[9,10] Impact can be further intensified through the use of sensor fusion, the combination of multiple sensing approaches, to gain more comprehensive insight into sample chemistry. Here, the combination of three types of optical spectroscopy, Raman, ultraviolet−visible (UV−vis) absorbance, and near-infrared (NIR) absorbance allows for rapid, noninvasive analysis of samples. These spectroscopies have been demonstrated to be highly valuable in the analysis of process streams containing multiple metal species in varied oxidation states,[11] and here they are applied to the microfluidic scale.

The use of UV−vis and NIR spectrometers provides an expanded range for absorbance spectroscopy in this study. NIR in particular has been underutilized on MFDs. NIR spectros-

Received: April 22, 2024
Revised: August 12, 2024
Accepted: August 20, 2024
Published: August 29, 2024

copy can provide rapid, noninvasive analysis of a wide variety of samples, often being applied in the food industry due to its ability to detect lipids, water, and organic functional groups found in food products.[12,13] NIR can also detect inorganic components, allowing its application in other fields such as nuclear reprocessing.[11] Handheld NIR instruments have been developed, allowing for on-site analysis,[12,14,15] making NIR spectroscopy a candidate for portable MFD platforms.[1,16] Though some absorption of NIR light occurs in certain polymers, the MFD material utilized here, poly(methyl methacrylate) (PMMA), is relatively transparent in the low NIR spectral range.[13] Another common MFD material, fused silica, transmits NIR light.[17] Despite transmissive MFD substrates being available and widely used, NIR has seen little application within the space of microfluidics compared to other techniques such as Raman and fluorescence spectroscopy.[18]

Coupled on the microfluidic device with UV−vis and NIR is Raman spectroscopy. Raman online monitoring processes have been developed to gather in situ analysis of samples, offering vibrational spectroscopic information on molecules at small scales.[19] Micro-Raman probes allow real-time vibrational spectroscopic measurement of solutions in narrow channels and small droplets.[5,7]

Many lanthanides are targets of great analytical interest in fields ranging from critical material harvesting to used nuclear fuel recycling, and they are used in green technology, biomedical applications, and nanotechnology.[20] Lanthanides exhibit similar chemistry, as most typically take a +3 oxidation state and have similar cationic size due to lanthanide contraction, making them difficult to physically separate from one another and from actinides exhibiting +3 oxidation states.[9,21]

Solutions containing multiple lanthanides or interfering species can produce complex optical spectra that become challenging to analyze. Chemometrics, a form of chemical data science, has been applied successfully in many cases to the complex data of optical spectroscopy.[11,12,15,22] Optical spectra can be analyzed via chemometric modeling to gain real-time analysis of chemical composition.[11] Chemometric analysis is a statistical method utilizing multivariate spectral signatures and correlated sample properties to create regression vectors by which sample properties can be measured from new spectra.[23] Here, multivariate analysis (PCR) is compared to univariate analysis (Beer's law) for the quantitative measurement of three lanthanide nitrates: neodymium (Nd), holmium (Ho), and samarium (Sm).

To demonstrate sensor performance under more static microfluidic specifications, chemometric models were created for each spectroscopy and path length individually. To demonstrate a more advanced sensor deployment, models were also created to incorporate absorbance spectra from the three optical pathlengths on the MFD. Other studies have examined methods for incorporating spectra collected at multiple pathlengths into a single model. Such methods include creating spectra from the slope of absorbance versus path length at each measured wavelength[24] and increasing model complexity to capture additional variability in multi-pathlength data sets.[25] Here, a small subset of samples are utilized to create a scaling vector for spectra collected in each of the three pathlengths. Finally, to demonstrate sensor fusion, spectra from the three optical methods are combined to create fused spectra from which chemometric models are built. The quantification of three lanthanides and their counterion, nitrate, is compared across the various models.

EXPERIMENTAL SECTION

Materials. Holmium nitrate salts ($Ho(NO_3)_3{\cdot}H_2O$, 99.9%) and samarium nitrate salts ($Sm(NO_3)_3{\cdot}3\ H_2O$, 99.9%) were sourced from Strem Chemical, Inc. Neodymium nitrate salts ($Nd(NO_3)_3{\cdot}6\ H_2O$, 99.9%) were sourced from Sigma-Aldrich. All solutions were prepared using ≥18.2 Ω·cm deionized water.

PMMA Microfluidic Device. The MFD consists of two fused plates of optically transparent PMMA. Within the body of the chip is a carved rectangular channel that takes several 90° turns between the inlet and outlet of the channel, forming three parallel tracks of channel which act as optical paths through which absorbance spectroscopy is conducted. The channels have printed pathlengths of 10, 2.5, and 1.0 mm, as shown in Figure 1C.[4]

Along the length of each channel is a narrow air space that acts as a mirror to guide light within the channel and prevent stray light. At each end of the channel is a convex pocket of air which acts as a two-dimensional lens to focus ingoing and outgoing light to and from bare optical fibers.[26] The bare fibers are inserted and secured with epoxy glue into guide paths,

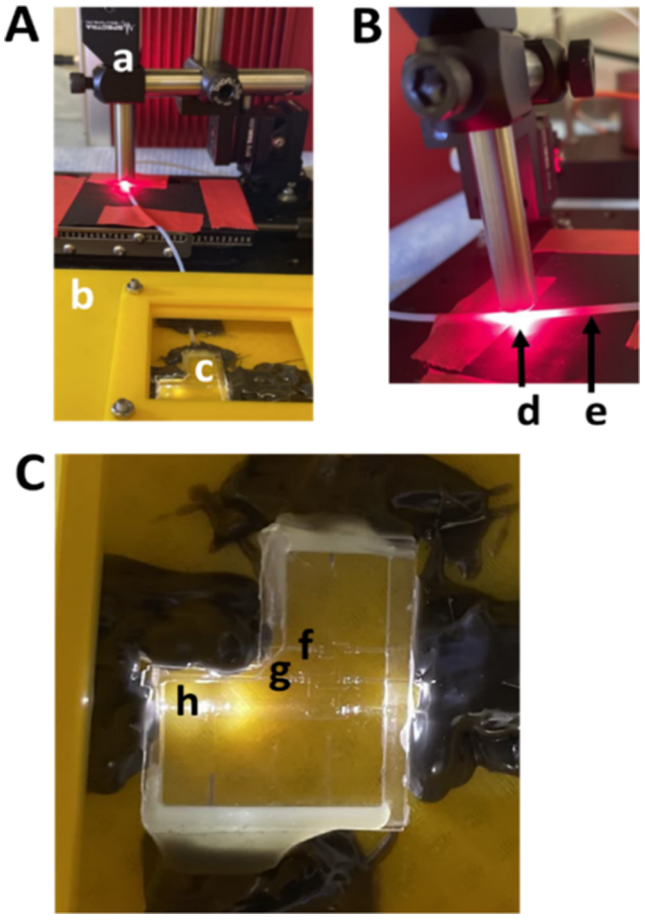

Figure 1. (A) Relative position of the (a) Raman probe during Raman spectral collection, (b) protective casing, and (c) microfluidic device with attached outlet tube. (B) Raman microprobe showing the (d) Raman laser focal point within the (e) outlet tube. (C) The PMMA microfluidic device shows (f) 1.0 mm, (g) 2.5 mm, and (h) 10 mm length optical channels, with excitation light directed through the 10 mm channel.

https://doi.org/10.1021/acsomega.4c03857
ACS Omega 2024, 9, 38548−38556

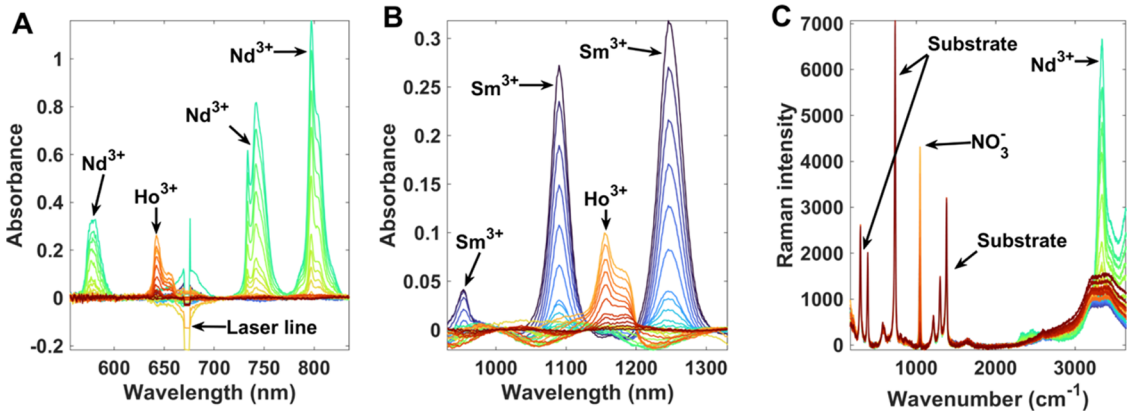

Figure 2. Spectral signatures of neodymium, holmium, and samarium nitrate in (A) UV−visible absorbance spectroscopy, (B) NIR absorbance spectroscopy, and (C) Raman spectroscopy. Spectra were preprocessed with a second-order polynomial baseline. Colors are used to distinguish spectra from one another and do not directly correlate to the analyte concentration.

which are aligned with the internal optical channels of the MFD. The fibers secured in the guide channels are ThorLabs M112L02 solarization-resistant fibers with a 200 μm core, a numerical aperture of 0.22, and a wavelength range of 180−1200 nm.

Spectrometers. All spectrometers were procured from Spectra Solutions, Inc. (Norwood, MA) and used associated Spectra Soft software (version 1.3).

Raman spectroscopy was performed using a 671 nm excitation laser, providing a resolution of approximately 5 cm^{-1} and an effective range of 166−3650 cm^{-1}. The detector consisted of a transmission volume phase holographic grating spectrograph with a thermoelectrically (TE) cooled charge-coupled device (CCD) to detect the Raman signal. The Raman microprobe shown in Figure 1B had a cross section of 70 μm.

UV−vis and NIR spectroscopies were performed on separate instruments. Each instrument used a TE-cooled CCD-based detector, providing an effective spectral range of 416−820 nm for UV−vis and 900−1700 nm for NIR. UV−vis and NIR light were provided by a tungsten-halogen SLS201L light source from ThorLabs (Newton, NJ), providing excitation light in the range of 360−2600 nm.

Spectral Collection. Integration times and the number of scans per sample varied per spectrometer. UV−vis and NIR were referenced to water, and integration times were optimized for maximum light transmission. 100 spectra were collected per sample on the UV−vis with an integration time of 0.8 s. 50 spectra were collected per sample for the NIR with an integration time of 1.0 s. Thirty spectra were collected per sample for the Raman with an integration time of 3 s. For data processing, spectra were averaged into 10 spectra per sample before quantification was performed.

Due to the shallowness of the MFD channel and the thickness of the top PMMA plate, the Raman signal from the Raman microprobe when focused into the MFD channel was dominated by the signal of the PMMA and did not adequately capture analyte signal. The Raman probe laser was aimed between the 2.5 and 10 mm channels during the collection of the UV−vis spectra to intentionally cause an interfering signal of the 671 nm laser in the visible spectra. After UV−vis and NIR spectra were collected, the Raman probe was focused within the outlet tube, which is contiguous with the flow from the MFD, and Raman spectra were collected for each sample; this arrangement is shown in Figure 1A. Future chip designs will accommodate the Raman capabilities on chip, allowing for simultaneous collecting of the three types of spectra.

Data Processing Software. Data was processed and plotted using MATLAB 2022b version 9.13 (Mathworks, Natick, MA) and PLS Toolbox version 9.1. (Eigenvector Research, Inc., Manson, WA).

Data Sets. Samples of single, binary, and tertiary lanthanide nitrate solutions were collected by using three spectroscopic methods. The samples were divided into calibration and validation data sets. The concentration profiles of the two data sets are shown in Figure S1.

Absorbance spectra were excluded from data sets when one or more constituents were above the linear concentration range of the constituent for that optical method. Tables S1−S4 list the maximum concentration for each analyte and the total number of spectra included in the calibration and validation data sets for each model. The exclusion of samples affects the standard deviation of the data set's analyte concentration, which affects the residual predictive deviation (RPD)[24] and the limit of detection (LOD) calculation.[27] This is discussed further in the Supporting Information.

Statistical Measures. Root-mean-square errors (RMSE) are commonly utilized as a measure of multivariate model uncertainty,[28] being considered a measure of absolute error for the model on the data set.[29] RMSEC is the root-mean-square error of the calibration set, and RMSEP is the root-mean-square error of the validation set. In other words, RMSEC measures the model's ability to fit the calibration samples, while RMSEP measures the model's ability to predict on new samples.[30] RMSE of cross-validation (RMSECV) is discussed in the Supporting Information.

RPD provides a measure of the model's robustness,[24] with higher RPDs indicating lower prediction errors relative to the inherent variability in the measured parameter. An RPD below 2 indicates an unreliable quantitative model, while an RPD between 2 and 3 indicates moderately reliable models.[24,31,32] RPDs above 5 indicate excellent models.[30,32]

LODs were calculated using a pseudo-univariate method from Allegrini and Olivieri.[27] This method of LOD generation is considered by some to be oversimple,[27,33] and it tends to overestimate LODs compared to more complex methods.[27] However, this method is independent of the number of variables (wavelength and wavenumbers) utilized in the models. Therefore, this method was chosen to compare

https://doi.org/10.1021/acsomega.4c03857
ACS Omega 2024, 9, 38548−38556

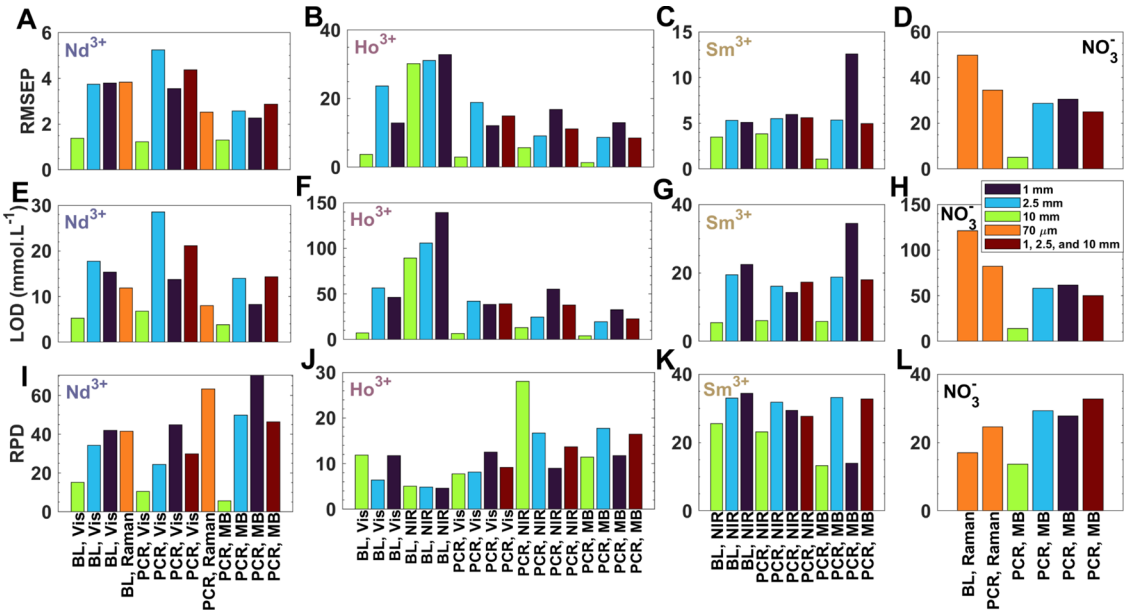

Figure 3. RMSEP for models of (A) Nd^{3+}, (B) Ho^{3+}, (C) Sm^{3+}, and (D) NO_3^-. Pseudo-univariate LOD was obtained from models of (E) Nd^{3+}, (F) Ho^{3+}, (G) Sm^{3+}, and (H) NO_3^-. RPD for models of (I) Nd^{3+}, (J) Ho^{3+}, (K) Sm^{3+}, and (L) NO_3^-. The legend in plot H applies to all plots and refers to optical pathlengths or beam width. BL = Beer's law regression, PCR = principal component regression, Vis = visible absorbance, NIR = near-infrared absorbance, and MB—multiblock. Nd—neodymium, Ho—holmium, Sm—samarium, NO_3^-—nitrate. RMSEP—root-mean-square error, LOD—limit of detection, RPD—residual predictive deviation.

LODs of univariate (Beer's law) and multivariate (PCR) models. This method is discussed further in the Supporting Information.

RESULTS AND DISCUSSION

Optical Spectra and Preprocessing. Figure 2A–C shows the UV–vis spectra of single-constituent solutions of neodymium, holmium, or samarium(III) nitrate; NIR spectra of the same samples; and Raman spectra, respectively. All metals were introduced as nitrate salts and therefore exhibit a nitrate signal within the Raman spectra at 1048 cm^{-1}. Neodymium produces strong absorbance signals in the visible region but also causes bands to grow in on top of the broad water signal in the Raman region from 2280 to 3642 cm^{-1}. Peaks on the plastic outlet tube are seen in the Raman spectra, as indicated in Figure 2C, but these are constant and insensitive to sample solution composition. Samarium cations produce strong signal in the NIR range. Holmium cations produce signal in both the visible and NIR ranges. In both ranges, the analyte signal is overlapped. The primary holmium band at 1157 nm sits between two strong samarium bands, the front and tail of which overlap with the holmium band. In the visible range (Figure 2A), the 671 nm Raman laser produces a strong signal, causing a sharp artifact with broad shoulders that overlaps the 642 nm holmium band. Random variation in the visible laser peak is due to laser power fluctuations, evidenced in Figure S2C as a slight baseline fluctuation. Further interferences can be noted in the raw absorbance spectra shown in Figure S2A,B, which display baseline offsets. Finally, Figure 2B shows nonlinear artifacts in the NIR baseline, which were inconsistent between the three pathlengths on the chip.

Spectra underwent one or more preprocessing steps prior to being modeled by a univariate or multivariate analysis. The spectra after preprocessing are shown in Figure S3. For UV–vis spectra, a Savitsky-Golay first derivative (15-point window, second-order polynomial) was used. For NIR spectra, a Whittaker filter (lambda of 15) and a Savitsky-Golay first derivative (15-point window, second-order polynomial) were applied. For Raman spectra, a Savitsky-Golay first derivative (15-point window, second-order polynomial) was applied. Two substrate peaks of the plastic tube were then used as normalization standards to correct for laser power fluctuations utilizing a 1-norm of the region under the areas of 250–440 and 1125–1430 cm^{-1}.

Several high-noise, nonanalyte regions are removed from the spectra before multivariate analysis occurred. Most notably, the laser line in the visible region is removed from UV–vis spectra, which also removes some holmium signal, and the sharp substrate peaks in the Raman spectra are excluded. The included regions for UV–vis multivariate PCR models are 556–666 and 681–835 nm. The analysis region for the NIR is 930–1330 nm. The analysis regions for Raman are 977–1104, 2215–2736, and 3088–3642 cm^{-1}.

For models that incorporated UV–vis and/or NIR spectra collected at multiple pathlengths, the following method was utilized to scale the spectra in order to reduce variation in absorbances caused by differences in the MFD's channels. For each spectroscopy, a scaling vector was created for the 10 and 2.5 mm pathlengths. An effective path length was determined relative to the 1.0 mm path length, according to eq S3. For UV–vis, spectra of 50.0, 75.0, and 100 mM $Nd(NO_3)_3$ solutions were utilized. For each sample, the absorbance value of 10 and 2.5 mm path length preprocessed spectra at 731 nm were ratioed to the absorbance of the 1.0 mm path length preprocessed spectra, producing a ratio of the effective pathlengths. The ratios calculated from the three samples were averaged for each path length. This process was repeated for NIR, using samples of 100, 200, and 300 mM $Sm(NO_3)_3$ measured at 1078 and 1235 nm, with ratios averaged across the two wavelengths. To account for absorbance baseline differences caused by fiber optic, channel, and chip wall thickness variations among the three pathlengths, a correction vector was

https://doi.org/10.1021/acsomega.4c03857
ACS Omega 2024, 9, 38548–38556

calculated relative to the 1.0 mm path length. A correction vector was calculated by taking the base-10 logarithm of the ratio of a single-beam water spectrum on the 1.0 mm path length divided by a single-beam water spectrum of the 2.5 or 10 mm path length, treating the 1.0 mm path length as if it were an absorbance reference. Finally, the sample spectra were divided by the difference of the effective path length and the correction vector for their respective path length. This resulted in spectra that were scaled to the 1.0 mm path length, without requiring *a priori* knowledge of the true, precise path length of any channel within the chip.

For multiblock data sets that combine UV−vis, NIR, and Raman spectra in a single model, spectra were scaled before being combined into data sets (shown in Figure S4). Scaling was conducted by taking the 1-norm of each spectrum for each spectroscopy, selecting the maximum 1-norm of the spectral matrix for that spectroscopy type, and dividing all spectra of the corresponding type by the maximum normalization scalar.

Before PCR was conducted, the spectral matrices were mean-centered. Concentration matrices were autoscaled in all models of nitrate, while the concentration matrices were otherwise mean-centered.

Univariate Analysis (Beer's Law). Univariate analysis was conducted at one wavelength for each analyte in each spectral type in which it produced a signal. Univariate analysis was performed using the Beer's law method, which relates spectral intensity to analyte concentration, as demonstrated in Figure S5. The model results of RPD, RMSEC, RMSEP, and LOD are shown in Table S1 for neodymium from UV−vis and Raman, in Table S2 for holmium from UV−vis and NIR, in Table S3 for samarium from NIR, and in Table S4 for nitrate from Raman. Results are shown visually in Figure 3, where it should be noted that low RMSEP and LOD (A−H) and high RPD (I−L) values are preferred.

The 10 mm path length in all cases provides the lowest LOD for the univariate analyses. The increased path length allows for more chromophores to enter the light path, ultimately resulting in an improved LOD. However, this results in light starvation at wavelengths where the analyte has a high molar absorptivity, resulting in a nonlinear relationship between the chromophore concentration and absorbance as concentration increases. The model of UV−vis spectra of neodymium collected on the 10 mm path length had the lowest upper limit of just 100 mmol L^{-1} $Nd(NO_3)_3$, whereas the maximum sampled concentration was 600 mmol L^{-1}. The upper concentration range is listed for all models in the tables in the Supporting Information.

Neodymium can also be effectively quantified using the 3286 cm^{-1} band in the preprocessed Raman spectrum, producing the second highest RPD in this study and similar statistics to the 2.5 and 1.0 path length UV−vis models. It should be noted that in more complex chemical systems, utilizing the Raman band may be challenging and that in organic phase systems, the band would not be present.

Samarium concentration is effectively quantified using the 1078 nm band in the preprocessed NIR spectrum. The RPD and LOD values increase from the 10 mm path length to the 2.5 mm path length, with a slight increase again in the 1.0 mm path length, but there is no definite relationship of RMSEP with path length. The univariate models function very well for samarium with only minimal improvements offered by multivariate models.

The chosen wavelength for holmium regression in the UV−vis region was 639 nm in the preprocessed spectrum. Univariate analysis could not account for the inconsistent, interfering laser signal, resulting in poor regression results for holmium compared with other models. In the NIR, the holmium concentration was quantified using the 1145 nm band in the derivative spectrum. Due to the front and trailing edge of the adjacent, high extinction coefficient samarium peaks, and the nonzero baseline, the NIR univariate regression of holmium performed extremely poorly relative to other models, producing RPD values below 5 (Figure 3J), LOD values above 80 mM (Figure 3F), and the highest RMSEs of any lanthanide model. The univariate models are unsuitable for the complexity of the holmium signal.

Multivariate Analysis (PCR). Multivariate analyses can incorporate an entire optical spectrum to quantify species in solution. In this work, multivariate analysis was performed by using PCR. PCR's ability to sequester noise and capture overlapping signal using regression vectors, called principal components (PCs),[34] allows for improved quantification compared to univariate Beer's law analysis in cases where optical signatures are confounded by variation that is independent of the target analyte's concentration, such as signals from other analytes or interferents, random noise, or baseline fluctuation.

All PCR models of a single spectroscopy type included only two principal components. By including only a small number of principal components in the final model, regression vectors capture primarily chemical variation, rather than noise or nonanalyte signal; the exclusion of excess PCs can result in more robust models while maintaining lower model errors compared to univariate models that do not exclude nonanalyte signals.[35] The third principal component in UV−vis and NIR models captured nonanalyte variation amounting to less than 1% variation in the spectral matrices, and therefore the third component was not deemed significant enough to warrant its inclusion.

The gravimetrically known concentrations for the three analytes versus the concentrations measured by the PCR model are shown in Figure S6, which also includes the best-fit lines and 95% confidence interval (CI) for the fits of the known and predicted concentrations. These plots are called parity plots. For nitrate and neodymium measured by Raman, the PCR model improves upon the univariate method significantly in every metric. For neodymium measured by UV−vis, performance varies compared to univariate analysis. For samarium, RMSEs remain similar to Beer's law analysis, LOD values remain similar or improved by PCR analysis, and RPD slightly decreases. For holmium, which displays the most spectral complexity, the PCR models offer significant improvement over the Beer's law models, with an improvement of up to 4.5 times in RMSEP. The greatest reduction in RMSE and LOD values is seen in the NIR models, for which spectral overlap and baseline effects are greatest.

There is not a proportional relationship between error and path length for the UV−vis and NIR spectroscopies in PCR, due to the unique array of nonchemical signals in the spectra on each path length. The 10 mm path length spectra produced the lowest LODs in the PCR models, as in the Beer's law models.

Multi-Pathlength (1.0 + 2.5 + 10 mm) PCR Models. The goal of quantifying spectra from all pathlengths using one model is to allow for simultaneous measurement and

https://doi.org/10.1021/acsomega.4c03857
ACS Omega 2024, 9, 38548−38556

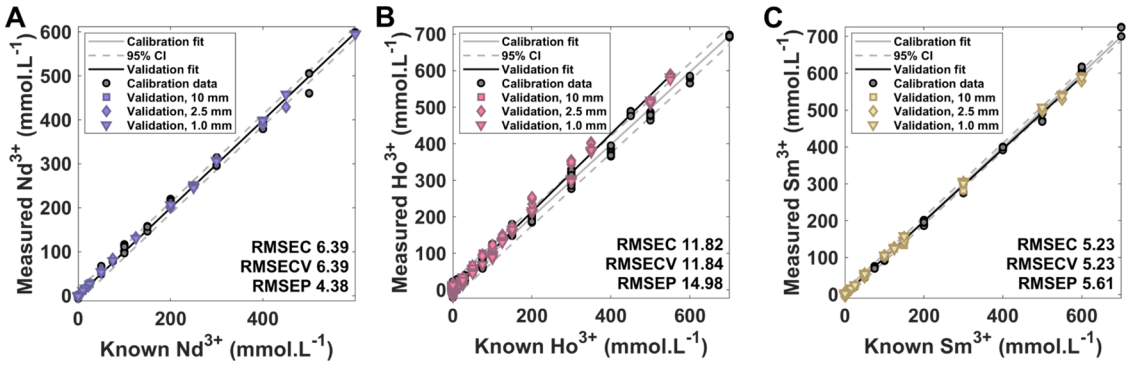

Figure 4. Parity plots of analyte concentrations determined gravimetrically and via principal component regression using data sets containing absorbance spectra collected at three pathlengths. (A) Neodymium measured from UV−visible spectra, (B) holmium measured from UV−visible spectra, and (C) samarium measured from NIR spectra. CI = confidence interval.

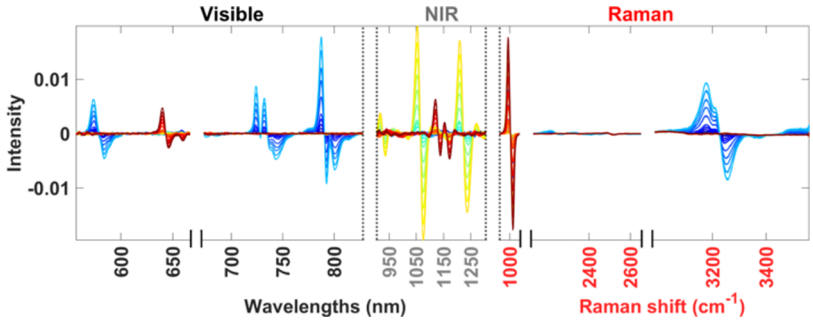

Figure 5. Preprocessed spectra of neodymium, holmium, and samarium nitrate solutions, showing visible absorbance, NIR absorbance, and Raman spectroscopy, concatenated into multiblock spectra. Axis breaks of two solid vertical lines indicate where wavenumbers or wavelengths were excluded from the multiblock data set, while vertical dashed lines indicate the boundaries between each spectral mode.

quantification of solutions at multiple physical locations in a system despite significant differences in the measurement conditions at those locations. The system here is a PMMA MFD and the differences in measurement condition are variation in optical path length, fiber optics, PMMA thickness, and detector arrays. Measuring at multiple locations that display great variability occurs also in process analytical technology (PAT) applications. Complex chemical processes may have unique measuring conditions at several locations in the system. If an analyst wishes to deploy a sensor using chemometric models into such a system, then the analyst must either create a calibration model for each measurement location or create a robust model that can analyze data from these disparate measurement conditions. It is the latter approach that is the focus of the following section.

UV−vis and NIR absorbance spectra were collected on three channels within the MFD, producing three spectra for each sample for each of these spectroscopies. These multi-pathlength data sets contain chemical variation, variation in analyte signal due to differences in the path length of absorbing solution, and differences in the signal-to-noise ratio. Slight differences in the reflectance, transmission, and absorbance of light by the chip itself along each of the three channels and the abutting chip body also introduce some variation. In the case of UV−vis spectroscopy, additional variation is introduced in the wavelength calibration that is unique to each optical path on the spectrometer itself, discussed in the Supporting Information. A model that incorporates spectra from all channels on the MFD must contend with all of these sources of variability.

Absorbance spectra from three pathlengths were assembled into data sets for each of the two spectroscopies separately, and spectra were scaled as described in the Optical Spectra and Preprocessing section. Statistics for multi-pathlength models are shown as dark red bars in Figure 3. Figure 4 shows parity plots of models of UV−vis and NIR data, using data sets that include unsaturated spectra collected at the three pathlengths.

For all three lanthanides in RMSEP, LOD, and RPD, the multi-pathlength PCR models produce statistics between those of the 2.5 and 1.0 mm path length models. The exception is the LOD for samarium, which is slightly higher in the multi-pathlength model than in either the 2.5 or 1.0 mm model. This middling performance indicates that, as expected, the multi-pathlength models cannot surpass the low RMSE or LOD of the 10 mm path length, yet these models retain comparable error to the models of the 2.5 and 1.0 pathlengths, despite the increased variance inherent in the multi-pathlength data sets. Further, the multi-pathlength models retain the wide concentration range and the high RPD of the 2.5 and 1.0 mm path length models, improving the multi-pathlength models' robustness compared to the 10 mm path length models.

Multiblock (UV−Vis + NIR + Raman) PCR Models. Multiblock modeling involves combining multiple sources of data measured from the same sample into a contiguous data set.[36] In this case, UV−vis, NIR, and Raman spectra were combined to form fused spectral matrices. Multiblock modeling provides benefits for the quantification of analytes that experience signal overlap in one type of spectroscopy but may be free of interference in another mode. It can also provide additional points of measurement for analytes that are

https://doi.org/10.1021/acsomega.4c03857
ACS Omega 2024, 9, 38548−38556

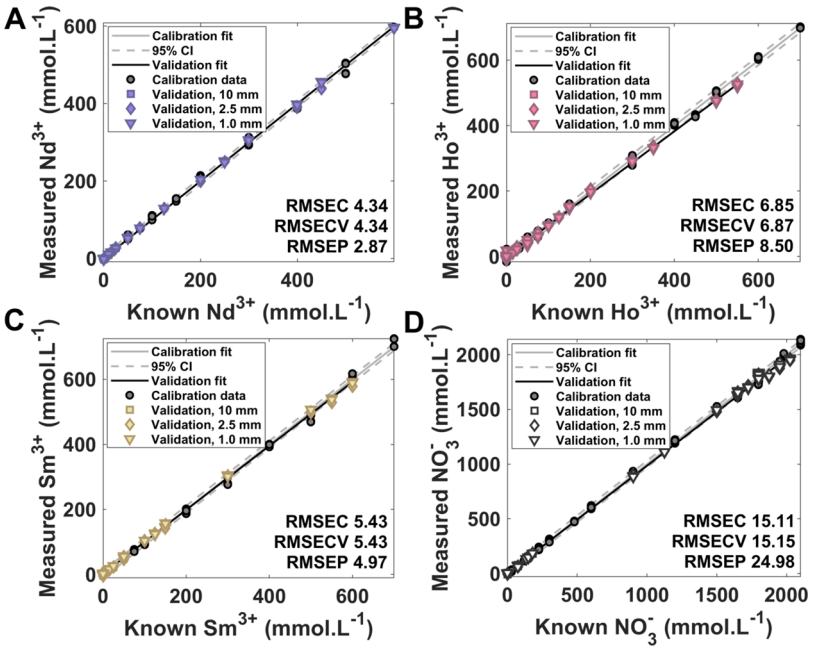

Figure 6. Parity plots of analyte concentrations determined gravimetrically and via principal component regression using data sets containing UV−visible and NIR absorbance spectra collected at three pathlengths and Raman spectra. (A) Neodymium, (B) holmium, (C) samarium, and (D) total nitrate. CI—confidence interval.

active in multiple modes. In this case, holmium and neodymium cations produce signal within the range of two spectroscopies each, whereas samarium and nitrate produce signal in one each. However, nitrate is covariant with all three lanthanide cations because the lanthanides are introduced as lanthanide (III) nitrates; this covariance allows for nitrate to be quantified from the signal provided by the lanthanide ions in the UV−vis and NIR spectra.

The multiblock spectra are shown in Figure 5. The model results are summarized and discussed below. Multiblock models included three principal components due to the three signal-producing analytes present in the merged spectra.

Neodymium produces strong signals in two spectral regions, allowing for an improvement in model results when both spectral modes are included in the spectral matrix. Multiblock models of neodymium are equivalent to or lower than single-spectroscopy models for RMSE and LOD values, and RPD values are in most cases higher than for single-spectroscopy models.

For holmium, RMSEC and LOD values are improved in every case by multiblock modeling, and RMSEP values are improved by multiblock modeling or are equivalent to the best single-spectroscopy modeling. The increase in net signal via the combination of the spectral signature in multiblock models compensates for the overlapping analytes and interfering signals that reduced the efficacy of holmium quantification from singular spectroscopy methods.

For samarium, multiblock modeling does not definitively improve quantitation. While the 10 mm path length model shows some improvement, the 1 mm path length model is markedly worse. Because samarium produced a signal only in the NIR range and produced a very strong signal in that range, a multiblock spectral matrix holds little additional information for the quantification of this analyte. The supplement of additional variables into a model quantifying samarium merely increases the non-samarium concentration variation which the model's PCs must capture, and this counteracts the typical benefit of a multivariate model.

In the case of nitrate, multiblock models produce in all cases lower RMSE and LOD values than single-spectroscopy models, and multiblock models produce higher RPDs except in the case of the 10 mm absorbance spectral data set. Nitrate is introduced into the system only in concert with the lanthanides. Therefore, even though holmium and samarium do not produce signals in the Raman spectra directly, their absorbance signals are still covariant with nitrate concentration. Therefore, by including the spectral regions of UV−vis and NIR, in which all three lanthanide cations produce a signal, the PCR model correlates the increase in nitrate with the corresponding increase in lanthanide signals, resulting in improved quantitation of the nitrate counterion.

Multiblock (UV−Vis + NIR + Raman) Multi-Pathlength (1.0 + 2.5 + 10 mm) PCR Models. Compared to multi-pathlength single spectral models, multi-pathlength multiblock models are either equivalent—in the case of samarium, or improved, in the cases of neodymium, holmium, and nitrate, for all statistical measures used in this study compared to single spectral models. Despite including the greatest amount of variation of any of the models examined thus far, these models perform very well, producing RMSEP and LOD values similar to or below those of the single-path length multiblock models. The RPD values of the multiblock multi-pathlength models are typically similar to or higher than many of the single-spectroscopy, single-pathlength models and are in every case higher than the single-spectroscopy, single-pathlength models, indicating the reliability of these models' quantitative predictions for the four analytes. The performance is reflected in parity plots in Figure 6 compared to Figure 4; in Figure 6, there is less divergence in samples measured on different pathlengths for neodymium (A) and holmium (B). The fit of the prediction also remains in closer agreement with the 95%

https://doi.org/10.1021/acsomega.4c03857
ACS Omega 2024, 9, 38548−38556

confidence interval of the calibration fit in the multiblock models than in the single spectral models.

CONCLUSIONS

Aqueous solutions of lanthanide nitrates were measured via UV−vis absorbance, NIR absorbance, and Raman spectroscopy on a custom PMMA MFD. Inset fiber optics allowed for simultaneous collection of absorbance spectra on three lengths of the channel within the MFD. An external Raman microprobe allowed for the collection of vibrational spectra on the connected outlet tube. Univariate and multivariate models allowed for the quantitation of lanthanide cations and counterions with low RMSE and high RPD values. Pseudo-univariate LOD allowed for comparison of LOD values across Beer's law and PCR analyses.

For the quantitative analysis of samarium, in which little spectral overlap occurs, the signal-to-noise ratio is high, and in which signal occurs in only one spectral mode, univariate calibration proved sufficient for quantification, with little improvement via PCR or multiblock PCR. Holmium prediction greatly improved through multivariate PCR, due to PCR's accommodation for baseline effects, spectral overlap, and lower signal-to-noise displayed by holmium in both UV−vis and NIR spectra. Multiblock modeling improved results for neodymium, holmium, and nitrate due to these analytes producing signals or having covariate signals in multiple spectroscopic modes. Multi-pathlength models were created which performed on par with single-pathlength models, despite a variance of up to 10 times in the optical path length of absorbance spectra. This study demonstrates how chemometric approaches enable the deconvolution of complex signals for the quantification of multiple analytes sampled under varied measurement conditions. It provides support for the development of complex sensor arrays in which sensors and calibration models can be deployed at multiple, unique locations in a system despite significant differences in measuring conditions at those locations. It demonstrates techniques useful for the analysis of solutions containing analytes that produce a high degree of spectral overlap or which have spectral signals confounded by matrix effects or concentration-dependent interactions.

ASSOCIATED CONTENT

Supporting Information

The Supporting Information is available free of charge at https://pubs.acs.org/doi/10.1021/acsomega.4c03857.

Discussion on the statistical measures used for model comparison; additional plots of raw and preprocessed optical spectra; tables of model statistics; and additional comparison of model results (PDF)

AUTHOR INFORMATION

Corresponding Authors

Hope E. Lackey − *Pacific Northwest National Laboratory, Richland, Washington 99352, United States; Department of Chemistry, Washington State University, Pullman, Washington 99164, United States*; Email: hope.lackey@pnnl.gov

Samuel A. Bryan − *Pacific Northwest National Laboratory, Richland, Washington 99352, United States; Department of Chemistry, Washington State University, Pullman, Washington 99164, United States*; orcid.org/0000-0002-8826-0880; Email: sam.bryan@pnnl.gov

Amanda M. Lines − *Pacific Northwest National Laboratory, Richland, Washington 99352, United States; Department of Chemistry, Washington State University, Pullman, Washington 99164, United States*; Email: amanda.lines@pnnl.gov

Authors

Alyssa F. Espley − *Pacific Northwest National Laboratory, Richland, Washington 99352, United States*

Savannah M. Potter − *Pacific Northwest National Laboratory, Richland, Washington 99352, United States*

Fabrice Lamadie − *CEA, DES, ISEC, DMRC, Univ Montpellier, 30207 Bagnols-sur-Cèze, France*; orcid.org/0000-0002-1449-5986

Manuel Miguirditchian − *CEA, DES, ISEC, DMRC, Univ Montpellier, 30207 Bagnols-sur-Cèze, France*

Gilbert L. Nelson − *The College of Idaho, Caldwell, Idaho 83605, United States*

Complete contact information is available at: https://pubs.acs.org/10.1021/acsomega.4c03857

Author Contributions

⊥H.E.L. and A.F.E. contributed equally to this work.

Notes

The authors declare no competing financial interest.

ACKNOWLEDGMENTS

This work was supported by the Office of Defense Nuclear Nonproliferation Research and Development within the U.S. Department of Energy's National Nuclear Security Administration. Research was performed at Pacific Northwest National Laboratory (PNNL), which is operated by Battelle Memorial Institute for the U.S. Department of Energy under contract DE-AC05-76RL01830. This work was supported in part by the U.S. Department of Energy, Office of Science, Office of Work-force Development for Teachers and Scientists (WDTS) under the Science Undergraduate Laboratory Internship (SULI) program. Microfluidic chip materials and setup were provided through collaboration with the CEA energy division in the framework of PRATA project.

REFERENCES

(1) Katla, S. K.; Zhou, W.; Tavakoli, H.; Méndez, E. L. P.; Li, X. Portable in situ temperature-dependent spectroscopy on a low-cost microfluidic platform integrated with a battery-powered thermofoil heater. *VIEW* **2023**, *4* (2), No. 20220053.

(2) (a) Beć, K. B.; Grabska, J.; Huck, C. W. Principles and applications of miniaturized near-infrared (NIR) spectrometers. *Chem. - Eur. J.* **2021**, *27* (5), 1514−1532. (b) Pandiselvam, R.; Prithviraj, V.; Manikantan, M.; Kothakota, A.; Rusu, A. V.; Trif, M.; Khaneghah, A. M. Recent advancements in NIR spectroscopy for assessing the quality and safety of horticultural products: A comprehensive review. *Front. Nutr.* **2022**, *9*, No. 973457. (c) Runowski, M.; Stopikowska, N.; Lis, S. UV-Vis-NIR absorption spectra of lanthanide oxides and fluorides. *Dalton Trans.* **2020**, *49* (7), 2129−2137.

(3) Launiere, C. A.; Gelis, A. V. High Precision Droplet-Based Microfluidic Determination of Americium(III) and Lanthanide(III) Solvent Extraction Separation Kinetics. *Ind. Eng. Chem. Res.* **2016**, *55* (7), 2272−2276.

(4) Rodríguez-Ruiz, I.; Lamadie, F.; Charton, S. Uranium(VI) On-Chip Microliter Concentration Measurements in a Highly Extended

UV-Visible Absorbance Linearity Range. *Anal. Chem.* **2018**, *90* (4), 2456−2460.
(5) Pinho, B.; Hartman, R. L. Microfluidics with in situ Raman spectroscopy for the characterization of non-polar/aqueous interfaces. *React. Chem. Eng.* **2017**, *2* (2), 189−200.
(6) El Maangar, A.; Theisen, J.; Penisson, C.; Zemb, T.; Gabriel, J. P. A microfluidic study of synergic liquid-liquid extraction of rare earth elements. *Phys. Chem. Chem. Phys.* **2020**, *22* (10), 5449−5462.
(7) Nelson, G. L.; Asmussen, S. E.; Lines, A. M.; Casella, A. J.; Bottenus, D. R.; Clark, S. B.; Bryan, S. A. Micro-Raman Technology to Interrogate Two-Phase Extraction on a Microfluidic Device. *Anal. Chem.* **2018**, *90* (14), 8345−8353.
(8) (a) Mattio, E.; Caleyron, A.; Miguirditchian, M.; Lines, A. M.; Bryan, S. A.; Lackey, H. E.; Rodriguez-Ruiz, I.; Lamadie, F. Microfluidic In-Situ Spectrophotometric Approaches to Tackle Actinides Analysis in Multiple Oxidation States. *Appl. Spectrosc.* **2022**, *76* (5), 580−589. (b) Yue, J.; Falke, F. H.; Schouten, J. C.; Nijhuis, T. A. Microreactors with integrated UV/Vis spectroscopic detection for online process analysis under segmented flow. *Lab Chip* **2013**, *13* (24), 4855−4863.
(9) Lackey, H.; Bottenus, D.; Liezers, M.; Shen, S.; Branch, S.; Katalenich, J.; Lines, A. A versatile and low-cost chip-to-world interface: Enabling ICP-MS characterization of isotachophoretically separated lanthanides on a microfluidic device. *Anal. Chim. Acta* **2020**, *1137*, 11−18.
(10) Hansen, E. H.; Miró, M. Interfacing Microfluidic Handling with Spectroscopic Detection for Real-Life Applications via the Lab-on-Valve Platform: A Review. *Appl. Spectrosc Rev.* **2008**, *43* (4), 335−357.
(11) Lines, A. M.; Hall, G. B.; Asmussen, S.; Allred, J.; Sinkov, S.; Heller, F.; Gallagher, N.; Lumetta, G. J.; Bryan, S. A. Sensor Fusion: Comprehensive Real-Time, On-Line Monitoring for Process Control via Visible, Near-Infrared, and Raman Spectroscopy. *ACS Sens.* **2020**, *5* (8), 2467−2475.
(12) da Silva Medeiros, M. L.; Cruz-Tirado, J. P.; Lima, A. F.; de Souza Netto, J. M.; Ribeiro, A. P. B.; Bassegio, D.; Godoy, H. T.; Barbin, D. F. Assessment oil composition and species discrimination of Brassicas seeds based on hyperspectral imaging and portable near infrared (NIR) spectroscopy tools and chemometrics. *J. Food Compos. Anal.* **2022**, *107*, No. 104403.
(13) Kradjel, C.; Lee, K. A. NIR Analysis of Polymers. In *Handbook of Near-Infrared Analysis*; CRC Press, 2007; pp 547−586.
(14) Salguero-Chaparro, L.; Palagos, B.; Peña-Rodríguez, F.; Roger, J. M. Calibration transfer of intact olive NIR spectra between a pre-dispersive instrument and a portable spectrometer. *Comput. Electron. Agric.* **2013**, *96*, 202−208.
(15) Wang, Z.; Wu, Q.; Kamruzzaman, M. Portable NIR spectroscopy and PLS based variable selection for adulteration detection in quinoa flour. *Food Control* **2022**, *138*, No. 108970.
(16) Akhtar, A. S.; Soares, R. R. G.; Pinto, I. F.; Russom, A. A portable and low-cost centrifugal microfluidic platform for multiplexed colorimetric detection of protein biomarkers. *Anal. Chim. Acta* **2023**, *1245*, No. 340823.
(17) Buchwald, K. *Fused Silica Transmission Gratings*; Ibsen Photonics, 2007.
(18) (a) Zhou, P.; He, H.; Ma, H.; Wang, S.; Hu, S. A Review of Optical Imaging Technologies for Microfluidics. *Micromachines* **2022**, *13* (2), No. 274. (b) Kuswandi, B.; Nuriman; Huskens, J.; Verboom, W. Optical sensing systems for microfluidic devices: A review. *Anal. Chim. Acta* **2007**, *601* (2), 141−155.
(19) (a) Das, A.; Fehse, S.; Polack, M.; Panneerselvam, R.; Belder, D. Surface-Enhanced Raman Spectroscopic Probing in Digital Microfluidics through a Microspray Hole. *Anal. Chem.* **2022**, *95* (2), 1262−1272. (b) Ochoa-Vazquez, G.; Kharisov, B.; Arizmendi-Morquecho, A.; Cario, A.; Aymonier, C.; Marre, S.; López, I. Microfluidics and surface-enhanced Raman spectroscopy: A perfect match for new analytical tools. *IEEE Trans. NanoBioSci.* **2019**, *18* (4), 558−566.
(20) Balaram, V. Rare earth elements: A review of applications, occurrence, exploration, analysis, recycling, and environmental impact. *Geosci. Front.* **2019**, *10* (4), 1285−1303.
(21) Zhang, H.; Wang, H.; Xu, H.; Zhang, L.; Xuan, J. Enabling separation intensification of a lanthanide pair with closely similar kinetics based on droplet microfluidics: hydrodynamic and kinetic approaches. *React. Chem. Eng.* **2019**, *4* (8), 1410−1420.
(22) Chapman, J.; Truong, V. K.; Elbourne, A.; Gangadoo, S.; Cheeseman, S.; Rajapaksha, P.; Latham, K.; Crawford, R. J.; Cozzolino, D. Combining Chemometrics and Sensors: Toward New Applications in Monitoring and Environmental Analysis. *Chem. Rev.* **2020**, *120* (13), 6048−6069.
(23) Kumar, N.; Bansal, A.; Sarma, G. S.; Rawal, R. K. Chemometrics tools used in analytical chemistry: An overview. *Talanta* **2014**, *123*, 186−199.
(24) Chen, B.; Wu, H.; Li, S. F. Y. Development of variable pathlength UV−vis spectroscopy combined with partial-least-squares regression for wastewater chemical oxygen demand (COD) monitoring. *Talanta* **2014**, *120*, 325−330.
(25) Hou, X.; Li, G.; Zhang, S.; Tian, H.; Feng, X.; Lin, L.; Fu, Z. Improving the spectral analysis accuracy of turbid solutions in flexible containers based on the CNCM theory. *Infrared Phys. Technol.* **2019**, *97*, 417−423.
(26) Rodríguez-Ruiz, I.; Ackermann, T. N.; Muñoz-Berbel, X.; Llobera, A. Photonic Lab-on-a-Chip: Integration of Optical Spectroscopy in Microfluidic Systems. *Anal. Chem.* **2016**, *88* (13), 6630−6637.
(27) Allegrini, F.; Olivieri, A. C. IUPAC-Consistent Approach to the Limit of Detection in Partial Least-Squares Calibration. *Anal. Chem.* **2014**, *86* (15), 7858−7866.
(28) Tse, P.; Bryan, S. A.; Bessen, N. P.; Lines, A. M.; Shafer, J. C. Review of on-line and near real-time spectroscopic monitoring of processes relevant to nuclear material management. *Anal. Chim. Acta* **2020**, *1107*, 1−13.
(29) (a) Westad, F.; Marini, F. Validation of chemometric models − A tutorial. *Anal. Chim. Acta* **2015**, *893*, 14−24. (b) Næs, T.; Martens, H. Multivariate calibration. II. Chemometric methods. *TrAC, Trends Anal. Chem.* **1984**, *3* (10), 266−271.
(30) Guerrero, C.; Mataix-Solera, J.; Arcenegui, V.; Mataix-Beneyto, J.; Gómez, I. Near-Infrared Spectroscopy to Estimate the Maximum Temperatures Reached on Burned Soils. *Soil Sci. Soc. Am. J.* **2007**, *71* (3), 1029−1037.
(31) Chang, C.-W.; Laird, D. A.; Mausbach, M. J.; Hurburgh, C. R. Near-Infrared Reflectance Spectroscopy−Principal Components Regression Analyses of Soil Properties. *Soil Sci. Soc. Am. J.* **2001**, *65* (2), 480−490.
(32) Zornoza, R.; Guerrero, C.; Mataix-Solera, J.; Scow, K. M.; Arcenegui, V.; Mataix-Beneyto, J. Near infrared spectroscopy for determination of various physical, chemical and biochemical properties in Mediterranean soils. *Soil Biol. Biochem.* **2008**, *40* (7), 1923−1930.
(33) Burgués, J.; Marco, S. Multivariate estimation of the limit of detection by orthogonal partial least squares in temperature-modulated MOX sensors. *Anal. Chim. Acta* **2018**, *1019*, 49−64.
(34) Lackey, H. E.; Sell, R. L.; Nelson, G. L.; Bryan, T. A.; Lines, A. M.; Bryan, S. A. Practical Guide to Chemometric Analysis of Optical Spectroscopic Data. *J. Chem. Educ.* **2023**, *100* (7), 2608−2626.
(35) (a) Wold, S.; Sjostrom, M. Chemometrics, present and future success. *Chemom. Intell. Lab. Syst.* **1998**, *44* (1−2), 3−14. (b) Rajalahti, T.; Kvalheim, O. M. Multivariate data analysis in pharmaceutics: A tutorial review. *Int. J. Pharm.* **2011**, *417* (1), 280−290.
(36) Borràs, E.; Ferré, J.; Boqué, R.; Mestres, M.; Aceña, L.; Busto, O. Data fusion methodologies for food and beverage authentication and quality assessment − A review. *Anal. Chim. Acta* **2015**, *891*, 1−14.

https://doi.org/10.1021/acsomega.4c03857
ACS Omega 2024, 9, 38548−38556